Imaging CSEM data in the presence of electrical anisotropy

Gregory A. Newman[1], Michael Commer[1], and James J. Carazzone[2]

ABSTRACT

Formation anisotropy should be incorporated into the analysis of controlled-source electromagnetic (CSEM) data because failure to do so can produce serious artifacts in the resulting resistivity images for certain data configurations of interest. This finding is demonstrated in model and case studies. Sensitivity to horizontal resistivity will be strongest in the broadside electric field data where detectors are offset from the tow line. Sensitivity to vertical resistivity is strongest for overflight data where the transmitting antenna passes directly over the detecting antenna. Consequently, consistent treatment of overflight and broadside electric field measurements requires an anisotropic modeling assumption. To produce a consistent resistivity model for such data, we develop and use a 3D CSEM imaging algorithm that treats transverse anisotropy. The algorithm is based on nonlinear conjugate gradients and full wave-equation modeling. It exploits parallel computing systems to effectively treat 3D imaging problems and CSEM data volumes of industrial size. We use it to demonstrate the anisotropic imaging process on model and field data sets from the North Sea and offshore Brazil. We also verify that isotropic imaging of overflight data alone produces an image generally consistent with vertical resistivity. However, superior data fits are obtained when the same overflight data are analyzed assuming an anisotropic resistivity model.

INTRODUCTION

New geophysical technologies can be combined with established seismic methods to improve the characterization of reservoir fluids in situations of practical interest. One technique that has emerged in the last several years uses low-frequency electromagnetic (EM) energy (less than 10 Hz) to map variations in the subsurface electrical resistivity of offshore oil and gas prospects (Eidesmo et al., 2002; El-lingsrud et al., 2002; Constable, 2006; MacGregor et al., 2006). In the marine controlled-source electromagnetic (CSEM) measurement technique, a deep-towed electric dipole transmitter is used to excite a low-frequency EM signal that is measured on the seafloor by electric and magnetic field detectors, with the largest transmitter-detector separations exceeding approximately 15 km. Electromagnetic (EM) data have been shown to be highly sensitive to changes in the pore-fluid types and the location of oil and gas accumulations, given that oil and gas are far more resistive than brine or water. The CSEM technique therefore has the potential to extract valuable information on reservoir fluid and rock properties that might not be sensed directly by seismic methods. The technique has been used to interrogate down to reservoir depths as deep as 4 km but benefits from structural information from seismic imaging to help delineate the bulk reservoir and surrounding geologic structure (cf. MacGregor et al., 2007).

Tompkins et al. (2004) and Tompkins (2005) recognize the importance of electrical anisotropy in the interpretation of CSEM data and this result could be anticipated from measurements made in deviated wells. Horizontally layered sedimentary sequences often arise in oil and gas exploration and can exhibit transverse anisotropy on a macroscopic scale — a scale much larger than individual sedimentary layers. Transverse anisotropy is the simplest case to model (cf. Newman and Alumbaugh, 2002). Fortunately, this corresponds to many situations encountered in actual geologic basins in which CSEM measurements are made for hydrocarbon exploration. Although it is possible to treat the more general form of the problem in which the formation anisotropy is modeled as a tensor with six independent elements (cf. Weiss and Newman, 2002), sedimentary formations are frequently horizontally layered or nearly so and the anisotropy can be described by independent vertical and horizontal resistivities. Although there are cases in which anisotropy is not vertically transverse and does not conform precisely to this scenario, vertical anisotropy still represents a significant improvement over an isotropic modeling assumption. Moreover, CSEM measurements could preclude the ability to map generalized anisotropy because of limited data coverage and acquisition geometry. Whether they can is an area of future research and is outside the scope of this paper.

Anisotropy can have a profound effect on CSEM measurements

and its effect depends strongly on acquisition geometry. The study of electrical currents in a double half-space by Lu and Xia (2007) is illuminating. Their model consists of an upper half-space that is isotropic (the sea water) and a lower half-space exhibiting transverse anisotropy (the sea bed). Vertical current flow and, hence, vertical resistivity have a much stronger impact on overflight electric-field measurements (null coupled data excluded); overflight data correspond to the case in which the CSEM tow line is over the detector. However, broadside measurements in which the measuring antenna is offset from and parallel to the tow line are far more sensitive to horizontal currents and, hence, the horizontal resistivity of the sea bed.

Large-scale 3D imaging is also receiving considerable attention in the interpretation of CSEM data (Carazzone et al., 2005; Plessix and van der Sman, 2007, 2008; Carazzone et al., 2008; Commer and Newman, 2008; Commer et al., 2008; Gribenko and Zhdanov, 2007; Plessix and Mulder, 2008; Zach et al., 2008). Although 1D modeling and inversion is relatively easy and trial-and-error 3D forward modeling is seemingly straightforward (Green et al., 2005; Hoversten et al., 2006; Weiss and Constable, 2006), the need for 3D imaging is necessary because the search for hydrocarbons now increasingly occurs in highly complex situations in which hydrocarbon effects are subtle aspects of the total offshore geologic environment. Further complicating matters is the realization that electrical anisotropy also needs to be incorporated directly into the imaging process (Carazzone et al., 2008; Jing et al., 2008; Newman and Commer, 2008). Failure to properly treat anisotropy can produce misleading and sometimes uninterpretable results when broadside data are included. Merely excluding broadside data-detecting antennas is frequently an issue when 3D coverage is desired.

In this paper, we introduce a 3D imaging approach that treats transverse anisotropy, which seems to be relevant for many practical exploration scenarios. We use it to study the imaging of electrical anisotropy in synthetic and field data set examples. The algorithm is based on nonlinear conjugate gradients and full wave-equation modeling and is an extension of an algorithm designed for 3D isotropic media (Commer and Newman, 2008). It exploits parallel computing systems to effectively treat large-scale 3D imaging problems and CSEM data volumes of industrial size.

IMAGING FRAMEWORK

In setting up the 3D imaging framework, we use finite-difference (FD) approximations to Maxwell's equations in the diffusive approximation for computing predicted data and cost functional gradients. The imaging problem is solved using a nonlinear conjugate-gradient scheme based on a regularized least-squares approach implemented on parallel computing systems. Many of the details of the 3D imaging approach adopted in this paper have been published elsewhere for the isotropic case (Newman and Boggs, 2005; Commer and Newman, 2008). An extension to treat the case of media exhibiting transverse anisotropy is not difficult and we provide a short discussion of the methodology here and in the appendix. For further technical details, we refer readers to the abovementioned works.

We seek to minimize the error functional

$$\phi = 1/2\{\mathbf{D}(\mathbf{d}^p - \mathbf{d}^{obs})^{\mathbf{T}}* \ \{\mathbf{D}(\mathbf{d}^p - \mathbf{d}^{obs})\}$$
$$+ \ 1/2\lambda_h\{\mathbf{Wm_h}\}^{\mathbf{T}}\{\mathbf{Wm_h}\} + 1/2\lambda_v\{\mathbf{Wm_v}\}^{\mathbf{T}}\{\mathbf{Wm_v}\},$$

$$(1)$$

where $\mathbf{T}*$ denotes the transpose-conjugation operator and $\mathbf{d}^{obs}$ and $\mathbf{d}^p$ the observed and predicted CSEM data, consisting of n complex values of electric and magnetic fields at the detectors. A diagonal weighting matrix $\mathbf{D}$ is incorporated into the error functional to help compensate for noisy measurements. Stabilization terms also appear in equation 1 and are designed to treat media exhibiting transverse electrical anisotropy. Parameterization of anisotropic electrical conductivity is made on a Cartesian grid, in which horizontal and vertical values are assigned to m cells — note that conductivity is the reciprocal of resistivity. Solution stabilization is achieved by reducing the model curvature in three dimensions in the minimization process. To do this, we use an FD approximation to the Laplacian (∇^2), producing a roughening matrix $\mathbf{W}$. Matrix $\mathbf{W}$ acts on the horizontal and vertical conductivity values $\mathbf{m_h}$ and $\mathbf{m_v}$, which are bounded using log or hyperbolic transformations. The regularization parameters λ_h and λ_v control the amount of smoothing admitted into the model for the two conductivities.

In modeling transverse anisotropy, an additional constraint is often imposed, $\mathbf{m_h} \geq \mathbf{m_v}$. The inequality is strictly valid for the case of thin vertical stacked layers that can be modeled as a parallel-serial circuit to electrical current flow in the horizontal and vertical directions. Although it is possible to enforce this inequality in the minimization of equation 1 with the parameterization

$$\mathbf{m_v} = \alpha\mathbf{m_h}; \quad 0 \leq \alpha \leq 1, \tag{2}$$

we do not enforce it in the results reported here. Sedimentary formations, although often layered, might not be sufficiently thinly layered for equation 2 to hold in general. Moreover, unlike well-logging problems in which measurements can be designed to sense variations in thin stacked layers along a well, CSEM measurements are made on the sea bed at a remote distance from such layering. They are not capable of distinguishing thin vertical variations in layering at the same resolution that can be recognized from induction logging. Nevertheless, for the problems discussed in this paper, we find equation 2 holds to a high degree even when the constraint is not explicitly enforced.

MODEL STUDY

Before presenting any field cases, model studies can yield important insight into interpreting the experimental results and can serve to properly set expectations. We consider a simple model to illustrate the key features in imaging data influenced by transverse anisotropic media. Because the CSEM method is designed to map resistors, we present models and imaging results that follow in the form of electrical resistivity instead of conductivity. The model shown in Figure 1 represents a simple reservoir model of 50 $\Omega \cdot$m isotropic resistivity. Its host medium exhibits transverse anisotropy, where horizontal (ρ_h) and vertical (ρ_v) resistivities are 0.65 and 2 $\Omega \cdot$m, respectively. The seawater resistivity is isotropic (0.3 $\Omega \cdot$m) and its depth is slightly more than 1 km. The model also exhibits a flat sea bottom with no bathymetry.

Data-acquisition geometry consists of 10 sail lines spaced at 1 km (Figure 2), where the transmitter transmits at 100-m intervals along each sail line at three frequencies: 1.25, 0.75, and 0.25 Hz. Twenty-five sea-bottom detectors on a uniformly sampled grid at 1 km are also shown. These detectors sample the horizontal electric fields in orthogonal directions E_x and E_y, whereas magnetic data are also recorded with field measurements, it has been our experience they offer little more information content than what is present in the electric

fields and will not be used here. Inline data (the null coupled data arising from detector antennas perpendicular to the sail line are discarded) and broadside data are present. For computational efficiency, we use reciprocity in which the detectors become the computational transmitters and the transmitters become the computational receivers. Numerical tests have demonstrated that the requirements of reciprocity are met to a satisfactory degree by the FD scheme used. Exploiting reciprocity results in 150 computational transmitters and 211,200 computational detectors.

In generating the synthetic data, we used a much finer grid — 201^3 nodes (cell size 50 m) — than used in the imaging experiments. Three simulation grids were used in the imaging, corresponding to 51^3, 81^3, and 101^3 nodes and assigned to frequencies 0.25, 0.75, and 1.25 Hz. The respective cell sizes for the simulation grids are 200, 125, and 100 m and are adapted to source frequency to meet the spatial sampling requirement of four grid nodes per skin depth. These grids are assigned to each computational transmitter depending on frequency and are used to compute predicted data and simulate fields within the medium. The grid used to render the image is finer than the simulation grids — 120^3 nodes. Separation of the imaging grid from the simulation grids results in significant acceleration in the computations. Interested readers are referred to Commer and Newman (2008) and the appendix for more details on the grid separation approach.

Five-percent Gaussian noise was added to the data and data amplitudes below an assumed noise floor of 1×10^{-13} were discarded. Data weighting was based on the amplitude of each data component to ensure that long offset data would make meaningful contributions in the error functional. In selecting the regularization tradeoff parameters λ_h and λ_v, we did not enforce directionally dependent smoothing on the model. Larger tradeoff parameters produce smoother images at the expense of an increase in the data-fitting errors and smaller tradeoff parameters produce the opposite. The choice of regularization parameters is dictated by the data noise and is optimally carried out using a cooling approach, in which initially large tradeoff parameters are selected and then systematically reduced until the data fit to the expected noise. This can lead to multiple inversion runs at considerable cost. For purposes here, we tested several values, settling on tradeoff parameters that were fixed to a value of 0.25.
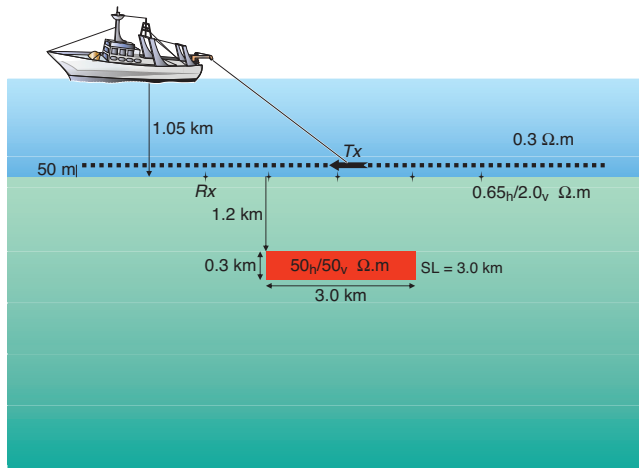
We carried out imaging of the data using two types of measurements: overflight and broadside data together, and overflight data only. This choice in considering two types of data is influenced by findings that broadside data with detectors parallel to the tow line are more sensitive to horizontal resistivity, much more so than overflight data (Commer et al., 2008). Using an isotropic starting model of $1 \, \Omega \cdot \text{m}$ for the sea bed, imaging results for a combination of overflight and broadside data (left panels) and only overflight data (right panels) are shown in Figures 3 and 4 in cross section and plan views. Enhanced resistivity of the reservoir zone is indicated in the vertical resistivity. Moreover, horizontal and vertical resistivities of the host medium are also captured within the sensitivity footprint of measurements. Footprints for vertical and horizontal resistivity illumination correspond to bowl-like structures; outside the illumination footprint there is little to no change in the resistivity from the starting model. These structures extend to several kilometers depth over the center of the tow lines and are more clearly rendered when the horizontal and vertical resistivity are plotted as a ratio (see Figure 5). The anisotropic imaging results show that treatment of overflight and broadside data renders sharper images than using data acquired only in the overflight mode. However, the overflight data produce a better depth estimate of the reservoir. This result arises because the imaging process was allowed to continue out to 250 iterations, compared to 100 iterations for the broadside and overflight data (see Figure 6). Improved depth resolution is observed as the problem is iterated.

Failure to image the reservoir is clear when inline and broadside data are treated assuming isotropic media. Rapid resistivity variations down to several hundred meters below the seafloor are observed, below which a low-resistivity feature several hundred meters thick is also indicated. The resulting data misfit (the data component part in equation 1) is unacceptably large (see the top plot in Figure 6), indicating the modeling assumptions are inadequate to image the data. Inspection of the data fits show that the cause for this poor result is due to the broadside data, specifically arising from de-

Figure 1. A simple 3D model to illustrate the key features in imaging data influenced by transverse anisotropy.
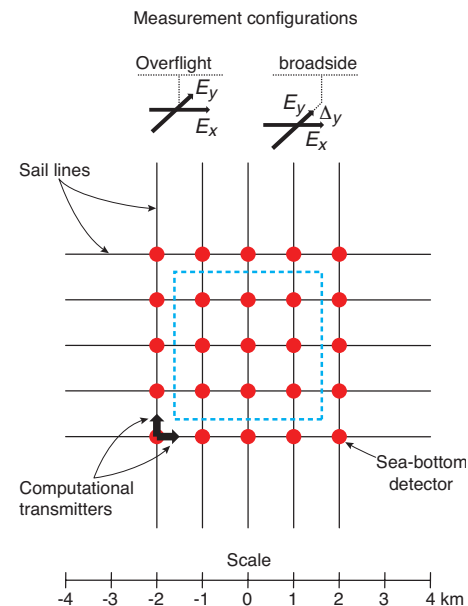

Figure 2. The data acquisition geometry consists of 10 sail lines spaced at 1 km. Twenty-five sea-bottom detectors are shown and the projection of the reservoir is indicated by the dashed square. Different measurement configurations are also illustrated.

tectors oriented parallel to the tow line. It confirms findings obtained from isotropic imaging of field data discussed below. Because inline broadside data are very sensitive to horizontal resistivity, failure to include anisotropy in the imaging process can produce disastrous image artifacts. However, the problem can be reduced by imaging only the overflight data. The result is illustrated in the right panels of Figures 3 and 4. Although still inferior to anisotropic imaging, enhanced resistivity is clearly associated with the reservoir. Thus overflight data are not that sensitive to horizontal resistivity but rather to vertical resistivity and can be imaged using an isotropic model, although image artifacts near the sea bottom remain. Data misfit is also much better in this case than when broadside and inline data are imaged assuming isotropic media (compare the corresponding top and bottom plots in Figure 6).

Results from this model study can be summarized as follows: With CSEM data, sensitivity to horizontal resistivity will be strongest in the broadside data with detectors parallel to and offset from the tow line and isotropic imaging assumptions can produce serious artifacts. Although it is possible to image vertical resistivity with overflight data and still extract useful information assuming an isotropic model, optimal results require a full treatment of anisotropic media within the imaging process.

FIELD EXAMPLES

Two field examples will now be presented. It is outside the scope of this paper to carry out a complete appraisal analysis of images
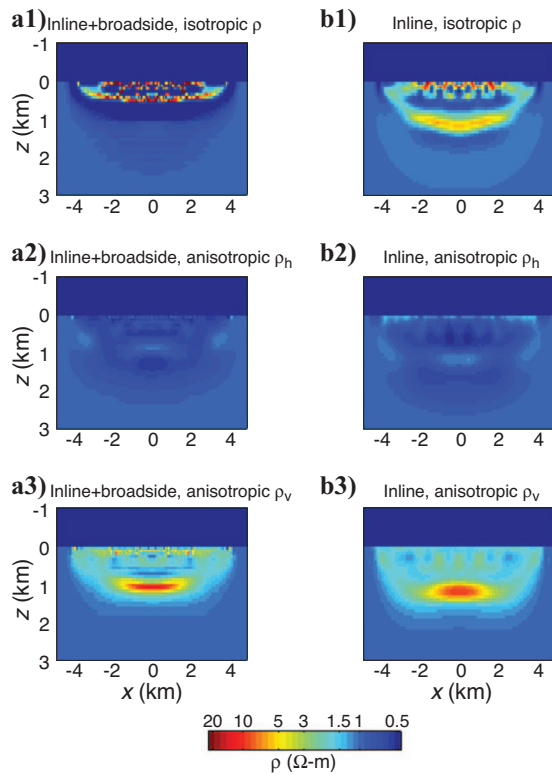

Figure 3. Imaged cross sections of the test model assuming isotropic and anisotropic media directly over the reservoir, $y = 0$ km. The left column considers overflight and broadside data. Those on the right are images based only on overflight data.
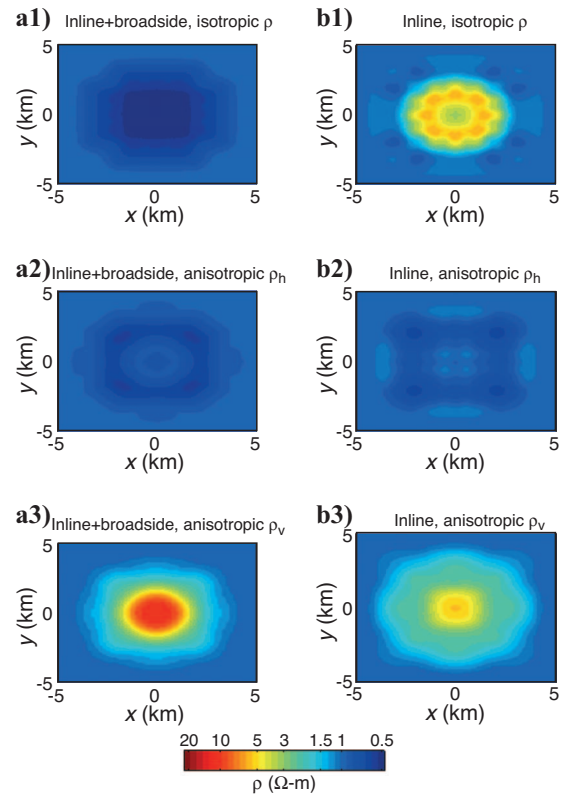

Figure 4. Imaged depth sections at 1 km of the test model data, assuming isotropic and anisotropic media. The left column considers overflight and broadside data. Those on the right are images based only on overflight data.
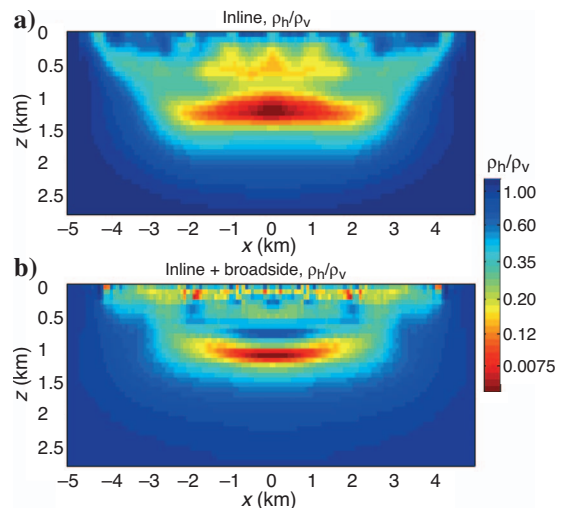

Figure 5. Cross-sectional ratio plots of horizontal (ρ_h) to vertical (ρ_v) resistivity of the test model directly over the reservoir, $y = 0$ km. Plots are based on inline and inline plus broadside data illustrated on a log scale. They were generated from the anisotropic imaging results of Figure 3. A value of 0.33 corresponds to the correct ratio for the background. Ratios near one indicate there is little change from the starting model and consequently the recovered model has little to no sensitivity to the data at these image points.

produced from field data. Such an analysis requires multiple inversions using different assumptions of data noise and weighting, regularization tradeoff parameters, and starting models. Tradeoffs between vertical and horizontal resistivity are certain to arise in the image process. The nature of these tradeoffs is difficult to quantify without a thorough appraisal study; therefore, our aim is more modest: to demonstrate that consistent anisotropic resistivity models can be produced that fit the observations better than isotropic models and to confirm findings from the model study. When features of the resistivity models can be verified with independent information, we will do so. Encouragingly, critical features of these models can be confirmed.
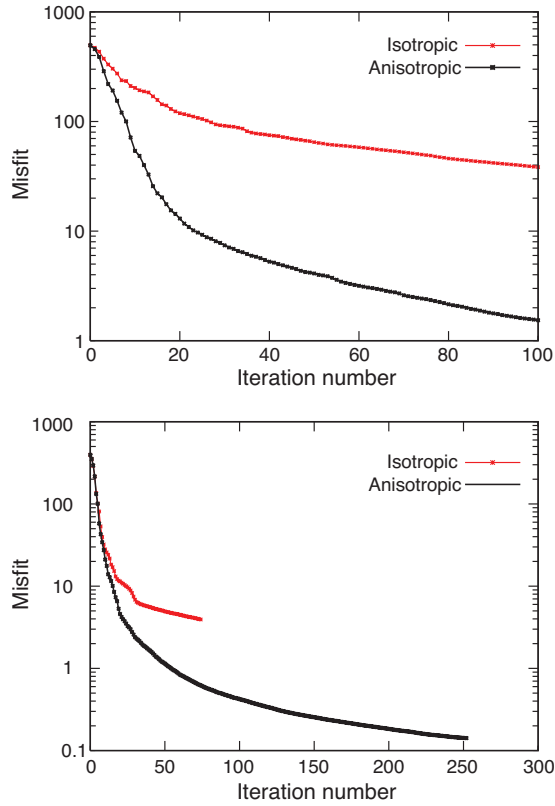

Figure 6. Convergence plots for isotropic and anisotropic media. The top plots show the data misfits plotted against inversion iteration for broadside and overflight data. Ideally, the target misfit is one assuming that the noise in the data is Gaussian. The lower plot is only for overflight data. Note also that number of iterations used for anisotropic imaging differs in the two plots.

Troll field

Controlled-source electromagnetic (CSEM) data acquired over the Troll West Gas Province (TWGP) have been used to vet isotropic imaging algorithms developed by various researchers (cf. Commer and Newman, 2008; Plessix and Mulder, 2008, Li et al. 2009, among others). Here we will use the data to verify results thus far developed from the model study for anisotropic media. The gas reservoir is located offshore Norway in the North Sea. A single 25-km-long sail line crosses over the reservoir with 24 CSEM electric field detectors spaced along 12 km of the line, over the gas field. The transmitter is towed in an overflight profile mode at an average height of 25 m above the seafloor. Seawater depth varies from 300 to 360 m over the sail line. Following Commer and Newman (2008), bathymetry effects are assumed to be minimal and ignored in the analysis. Data at two frequencies were used — 0.75 and 0.25 Hz. Simulation meshes used for the two frequencies are based on skin depth estimations, as discussed earlier. A separate simulation mesh is assigned to each source in practice and is adapted to the source and receiver positions and their corresponding offsets. The meshing is summarized in Table 1 along with the imaging mesh. We also used the same type of data amplitude weighting and the noise floor assumptions for the field data as was done in the model study and by Commer and Newman's (2008) earlier investigation. Vertical and horizontal regularization tradeoff parameters were fixed at 0.1 and are also based on the tradeoff parameter that was used in the analysis of the Troll data that assumed an isotropic resistivity model. Additional details on the Troll survey logistics and the setup of the imaging experiment can be found in Johansen et al. (2005).

Figure 7 compares imaging results for anisotropic and isotropic media along with an interpreted geologic section published by Johansen et al. (2005), based principally on well-log and seismic data. Isotropic and anisotropic (vertical resistivity) models clearly image the gas field and correspond closely to the geologic section. Even though we failed to achieve the target misfit of one (Figure 8), the anisotropic inversion produced a model that yields good data fits and a lower misfit error. Sensitivities to horizontal and vertical resistivity variations are observed and it appears that the isotropic imaging attempts to merge these disparate resistivities into a single image. It is tempting to assign low-resistivity features to horizontal resistivity variations but a detailed appraisal study is needed to make a determination. These features could also arise from a tradeoff between vertical and horizontal resistivity parameterization and from stabilization/regularization used in the imaging. Down to 1-km depth below the sea bed, we observed much less variation in the vertical and horizontal resistivities than in the isotropic case; at the seafloor we observed resistivity variations for isotropic and anisotropic cases. We believe this is caused by detector positioning errors and high sensitivity in the imaging to near sea-bottom resistivity variations. Aniso-

Table 1. List of model and simulation grids for the Troll data inversion. The variables Ω_{m} and Ω_s^1 and Ω_s^2 correspond to the modeling mesh and the two simulations meshes designed for frequencies 0.25 and 0.75 Hz. Grid sizes are in meters.

Grid	Number of cells	Δx	Δy	Δz	
Ω_{m}	$125 \times 41 \times 59$	250	250	100	
		$\Delta_x^{\min}/\Delta_x^{\max}$	$\Delta_y^{\min}/\Delta_y^{\max}$	$\Delta_z^{\min}/\Delta_z^{\max}$	$f\,(\mathrm{Hz})$
Ω_s^1	$85 \times 41 \times 85$	125/250	250/250	25/200	0.25 (f1)
Ω_s^2	$110 \times 43 \times 85$	75/125	125/250	25/200	0.75 (f2)

tropic imaging of the Troll data shows intriguing and consistent results. Even in anisotropic imaging of the overflight mode, lower data-fitting errors are observed compared to isotropic imaging of the data.

Campos Basin

The Campos Basin, located offshore Brazil, is a known oil and gas province with ongoing production. In 2004, a first-of-its-kind 3D CSEM survey was carried out to better quantify the hydrocarbon potential over part of the basin. Analysis of the Campos Basin data including the broadside measurements without taking anisotropy into

account produced serious image artifacts (Commer et al., 2008). It was demonstrated that inline broadside electric-field data were particularly sensitive to horizontal resistivity and could not be interpreted with an isotropic model. Carazzone et al. (2008) present 3D anisotropy imaging results of Campos Basin data. With the treatment of anisotropy, 3D imaging of the electric field data produced interpretable results. Here we will review the findings of these works, focusing on the importance of anisotropy in the imaging process.

The Campos Basin data were acquired using 10 sail lines at 5-km intervals (Figure 9), resulting in data acquisition from nearly one million transmitter sites using three frequencies: 1.25, 0.75, and 0.25 Hz. Twenty-three detectors were deployed on the seafloor on a 40×40 km^2 grid. Horizontal grid sizes used in the imaging mesh
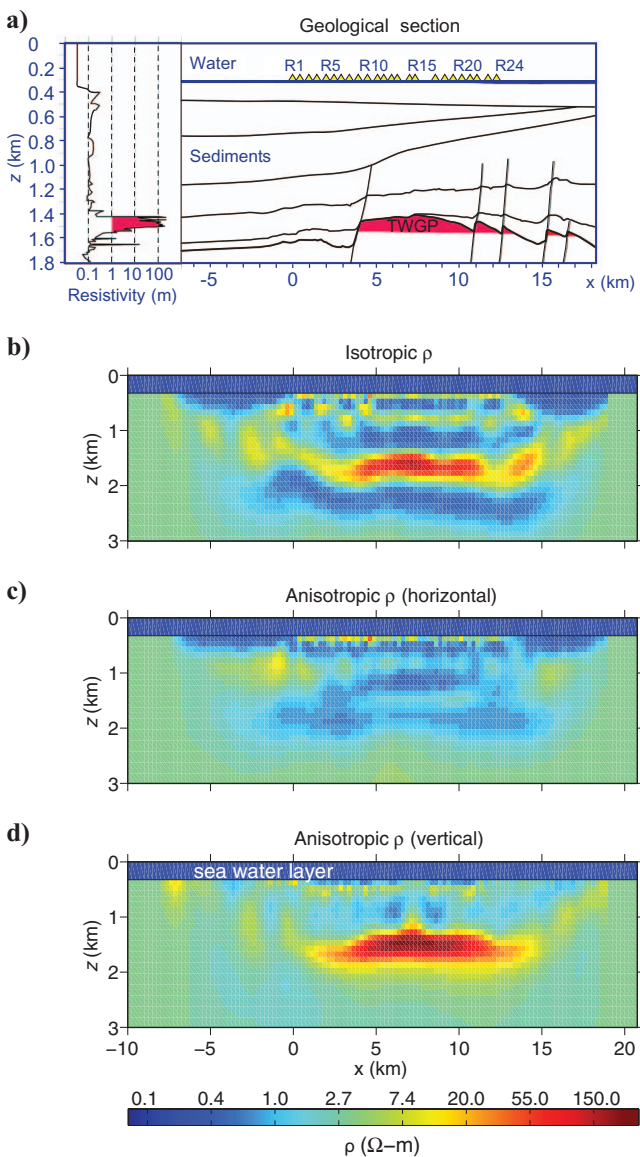

Figure 7. Imaging results for the Troll field. The top part of the figure is the interpretation published by Johansen et al. (2005) based on well-log and seismic data. The middle and lower panels show the isotropic and anisotropic CSEM imaging results.
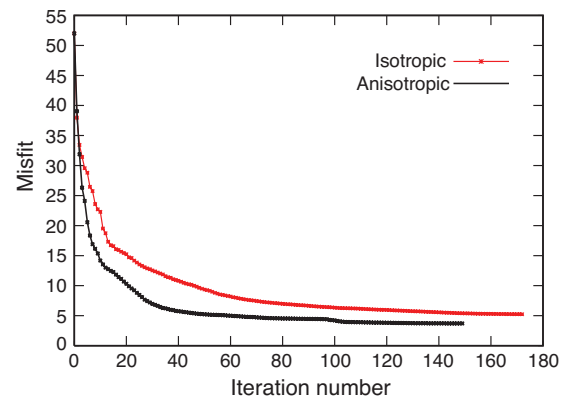

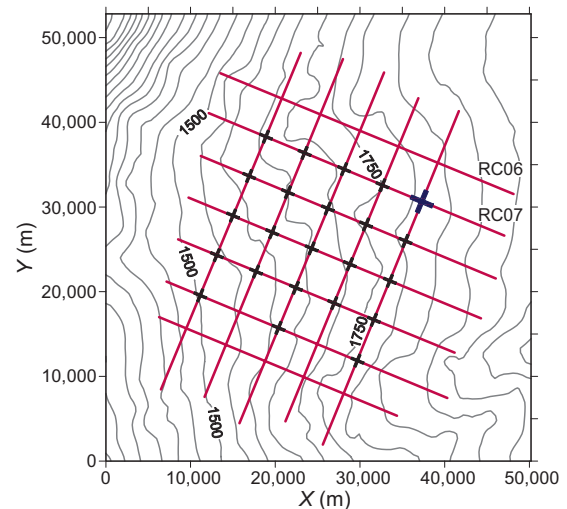Figure 8. Convergence plots for isotropic and anisotropic media for the Troll data set.

Figure 9. Shown are the layout of the sail lines and 23 sea-bottom detectors indicated by the plus symbols for the Campos Basin CSEM survey. The bathymetry is in meters below sea level with a contour interval of 50 m. Data acquired at the detector in bold, shown closest to the upper right-hand corner of the plot, is used to illustrate the data-fitting errors for broadside and overflight data in Figure 10 along sail lines RC06 and RC07.

were kept constant at $\Delta = 250$ m and vertical meshing varied from 40 to 200 m depth. Thus the total number of nodes used in the meshing was 403 along x and y and 173 nodes vertically, which corresponds to 27.8 million cells. Horizontal meshing for field simulation was designed on the criteria that from each computational source midpoint, 10 skin depths were spanned assuming 2-$\Omega \cdot$ m resistivity for the sea bed. Grid sizes varied with frequency and were set to $\Delta = 250$ m, 200 m, and 125 m, according to frequency $f = 0.125$ Hz, 0.25 Hz, and 0.5 Hz, respectively. Vertical meshing for simulation was identical to that in the image mesh to account for an accurate representation of the seafloor bathymetry. With these considerations, the size of the simulation meshes was reduced significantly; the number of x and y grid nodes range from 128 to 162. Solution accuracy was also verified against solutions in which simulation and imaging meshes were identical.

Overflight and broadside electric field data were imaged from this experiment using fixed tradeoff parameters $\lambda_h = 0.025$, $\lambda_v = 0.025$, and $\lambda = 0.25$ for the isotropic case. A detailed 3D starting model was constructed from forward modeling of the data. To preserve key features of the starting model in the imaging process, it was necessary to avoid setting the regularization parameters too large because large parameters smooth out the resistivity image. We also avoided making them too small to ensure a stable image. Data weighting used was based on the amplitude of the total electric field at each computational detector to reduce the sensitivity of weakly coupled data in the inversion process. Again, reciprocity processing was used to reduce the number of computational transmitters. All three components of the electric field were included in the data analysis. Shown in Figure 10 are data fits for isotropic and anisotropic modeling assumptions along selected profiles. The isotropic results presented by Commer et al. (2008) show that it is possible to fit the overflight data and broadside perpendicular and vertical data as the problem is iterated but not the broadside data arising from the detectors parallel to the tow line (inline components). A systematic fitting error is observed with broadside inline data displays, which does not dissipate as the problem is iterated. This indicates a bias in the underlying assumptions used in the image processing. However, overflight and broadside inline data can be fit with an anisotropy model. These results confirm that the broadside data, particularly the inline detector components, are quite sensitive to horizontal resistivity and other data components to vertical resistivity.

Commer et al. (2008) show that the resistivity images created by the isotropic media produced strong data-acquisition overprints, particularly near the seafloor, and other nongeologic effects proceeding to significant depths (this resistivity image is shown in Figure 11). Subsequent modeling by Commer et al. (2008) also confirms that improved broadside data fits (inline data) can be achieved by considering the medium that exhibits transverse anisotropy. A complete anisotropic inversion of the data was carried out by Carazzone et al. (2008). As expected, anisotropic resistivity imaging eliminates the problems observed with isotropic resistivity assumptions. Although the resistivity interpretation by Carazzone et al. (2008) does not directly reveal hydrocarbons, they demonstrate many correlations between the resistivity and seismic images that high-graded the hydrocarbon potential. Shown in Figure 12 is a vertical resistivity transect across a known hydrocarbon reservoir with the seis-
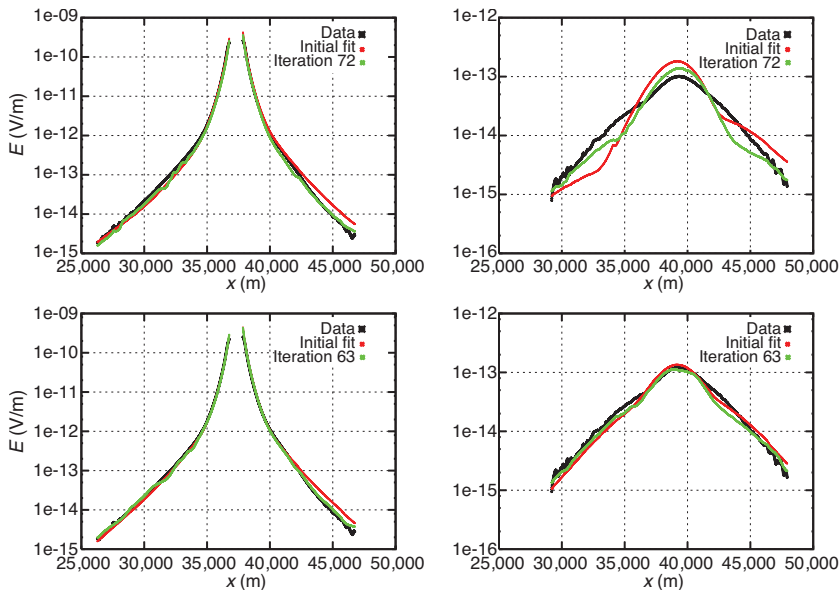

Figure 10. Plotted are data fits to overflight data (line RC07; upper left shows isotropic and lower left shows anisotropic) (line RC06; upper right shows isotropic and lower right shows anisotropic). Data acquired at the detector in bold and the plots are projected along the x axis (see Figure 9). The observed data are plotted in black, the predicted data at iteration 72 and 63 in green, and the predicted data for the starting model in red. The data correspond to a frequency of 0.125 Hz. The anisotropic starting model uses a vertical resistivity identical to that used in the isotropic imaging. However, the horizontal resistivity was set to one third the vertical resistivity below the water bottom.
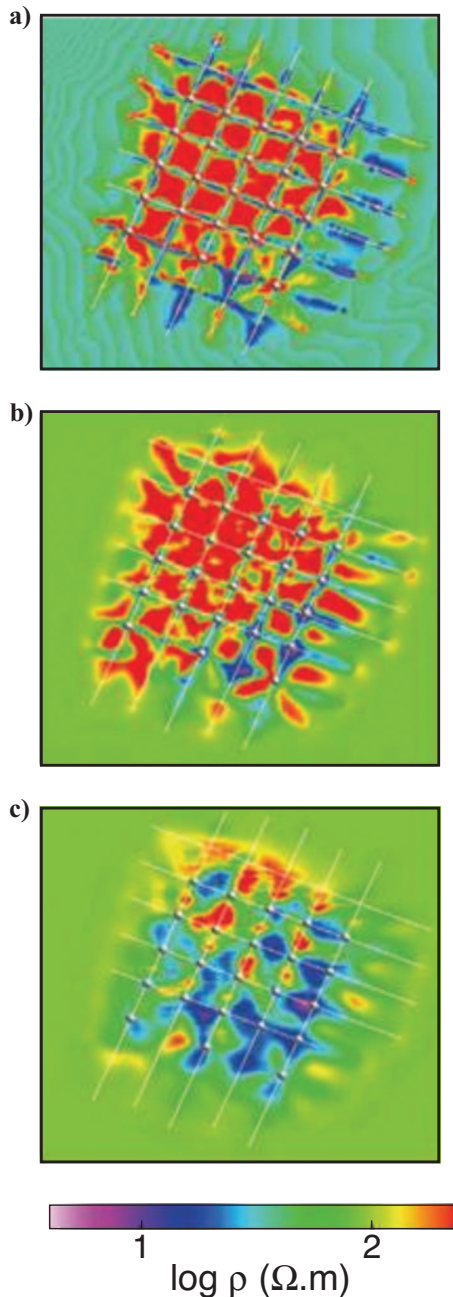
a)

b)

c)

$$\log \rho \ (\Omega.m)$$

Figure 11. Shown is the average resistivity computed over three depth ranges assuming an isotropic medium. The figure is from Commer et al. (2008) and shows (a) average resistivity from the water bottom to 500-m depth, (b) depth interval 500 to 1500 m, and (c) 1500 to 2500 m. Resistivity is rendered on a base 10 log scale.

mic image superimposed. The combined image shows three interesting features. Anomaly A points to a resistivity enhancement associated with a known oil field below a seismically imaged fault. At anomaly B, the resistivity enhancement is associated with a possible trap above a salt diapir with stratigraphic pinchouts and faulting. Lastly, anomaly C shows a possibility of conductive brine leaking up from deeper salt. Although salt is considered resistive, brines originating from it can be conductive. Such brines can be buoyant and rise from depth because of dissolved gas.
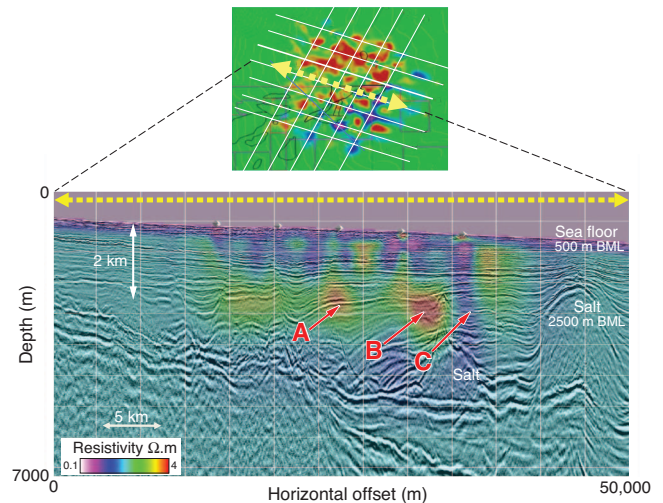

Figure 12. Rendered at the top is the average vertical resistivity map from 500 to 2500 m below the seafloor, superimposed with sail lines used to acquire the Campos Basin data. Also shown are lease block boundaries outlined in violet and known hydrocarbon deposits (black contours). The cross-section at the bottom shows the vertical resistivity image along the indicated transect. The EM image is shown together with seismic-reflection horizons. Results are presented by Carazzone et al. (2008).

CONCLUSIONS

The algorithm introduced in this paper has been designed to treat 3D resistivity media exhibiting transverse anisotropy. Within the stated modeling assumptions, this algorithm is sufficiently general and can treat large-scale imaging problems and industrial-sized data volumes critical for 3D CSEM resistivity imaging. There are also several extensions to the algorithm worth mentioning. Joint imaging of CSEM and magnetotelluric (MT) data has much appeal as MT data acquisition comes at little additional cost and can significantly improve resolution of the resistivity image (cf. Commer and Newman, 2009). Our approach to imaging 3D transverse anisotropy is easily extended to a joint imaging framework for CSEM and MT data. In fact, we have already implemented it. An extension to treat 3D media exhibiting generalized anisotropy is also possible but will require six resistivity estimates per image cell. We doubt that all six parameters can ever be resolved given the additional number of degrees of freedom but future research on the problem might prove otherwise. The results from the Campos Basin study are encouraging in this regard. Clearly, the anisotropy present is not strictly transverse given how salt and faulting has distorted the geologic bedding planes yet a transverse anisotropic resistivity model is sufficient to fit the data and has resistivity features that are geologically consistent with well information and seismic imaging results. Perhaps the description of the resistivity with horizontal and vertical resistivity is sufficient here because the model is represented by cell values on a grid. Because the cell size is much smaller than the skin depth, the modeled anisotropy at the skin-depth scale is quite general.

Case and model studies confirm the importance of electrical anisotropy in imaging CSEM data. The presence of anisotropy can be confirmed when overflight and broadside electric-field measurements are found to be inconsistent with an isotropic resistivity model. Electric field data acquired in the broadside configuration using inline detectors are particularly sensitive to horizontal resistivity.

High sensitivity to vertical resistivity is observed for overflight electric field data and broadside vertical and perpendicular data to some extent. Isotropic imaging using such data can yield meaningful results with respect to vertical resistivity (broadside measurements omitted) because there is less sensitivity to horizontal resistivity variations. Nevertheless, we find that anisotropic imaging of these data produces superior results as measured by better data fits and more consistent resistivity models.

APPENDIX A

3D CSEM INVERSE MODELING: TREATING TRANSVERSE ANISOTROPY

Minimization of equation 1 is carried out using a nonlinear conjugate gradient scheme with a line search to control the model step. Typically, only three to four solutions of the forward-modeling problem for each transmitter and excitation frequency are necessary to obtain the model update. This iterative scheme is ideal for large-scale data sets and imaging volumes that typically arise for CSEM problems. The solution for isotropic media has been developed by Commer and Newman (2008) and Newman and Boggs (2005). Here we will discuss modifications to the abovementioned approach for media exhibiting transverse anisotropy.

Large computational demands arise in solving realistic 3D CSEM field simulation problems. In solving such problems, we use FD approximations over a simulation mesh because of their simplicity and accuracy. Now the simulation mesh Ω_s is not required to be identical to the mesh Ω_m used for the inverse modeling. Hence, significant computational efficiencies can be realized when the meshes are different for large-scale problems (cf. Commer and Newman, 2008). The solution of the forward problem is obtained through a sparse linear system of equations

$$\mathbf{KE} = \mathbf{S}. \quad \text{(A-1)}$$

It is solved using iterative Krylov methods (cf. Newman and Boggs, 2005). With 13 nonzero entries per row, $\mathbf{K}$ is a sparse complex symmetric matrix, $\mathbf{E}$ is the electric field sampled on the mesh using a staggered grid (Yee, 1966), and $\mathbf{S}$ is the field sourcing term, with Dirichlet boundary conditions imposed in equation A-1.

This matrix equation is a discrete representation of the operator

$$\nabla \times \nabla \times E^S + i\omega\mu_o\underline{\sigma}E^S = -i\omega\mu_o(\underline{\sigma} - \underline{\sigma}^b)E^b, \quad \text{(A-2)}$$

where

$$\underline{\sigma} = \begin{pmatrix} \sigma_h & 0 & 0 \\ 0 & \sigma_h & 0 \\ 0 & 0 & \sigma_v \end{pmatrix} \quad \text{and} \quad \underline{\sigma}^b = \begin{pmatrix} \sigma_h^b & 0 & 0 \\ 0 & \sigma_h^b & 0 \\ 0 & 0 & \sigma_v^b \end{pmatrix} \quad \text{(A-3)}$$

Equation A-2 is a 3D vector equation for the scattered electric field arising in conductive media exhibiting transverse anisotropy. It assumes a time harmonic dependence of $e^{+i\omega t}$, where ω represents angular frequency and $i = \sqrt{-1}$. The electrical conductivity $\underline{\sigma}$ is described by a tensor, where σ_h and σ_v denote the conductivities in the horizontal and vertical directions; magnetic permeability μ_o is assumed to be that of free space. We prefer a scattered field solution to the field equations over a total field because of accuracy issues, particularly in the vicinity of the transmitter. In a scattered-field formulation, we are also required to specify a background electric field E^b. Thus the total electric field is given by $E = E^b + E^s$. Here we have selected a background field arising from 1D layered media that also exhibits transverse anisotropy $\underline{\sigma}^b$. The background field can be easily and quickly computed from Hankel transforms. Once the electric field is determined from equation A-1, the magnetic field follows from Faraday's law by numerically approximating the curl of the electric field at the various nodal points and interpolating these fields to the points of interest. In a scattered field formulation, background fields will need to be added to the interpolated fields to yield the total fields.

Following Commer and Newman (2008), the inversion unknowns $\mathbf{m_h}$ and $\mathbf{m_v}$ belong to Ω_m and a mapping is required from Ω_s to Ω_m in computing the gradient of equation 1. This gradient is used to update the conductivity model in the inversion process using the nonlinear conjugate-gradient scheme previously mentioned. Consider the data component of the gradient $\nabla\varphi_d(\mathbf{m_h},\mathbf{m_v})$, which involves only the first term in equation 1,

$$\nabla\varphi_d(\mathbf{m_h},\mathbf{m_v}) = -Re\{(\mathbf{DJ}^T)\mathbf{D}(\mathbf{d^p} - \mathbf{d^{obs}})^*\}. \quad \text{(A-4)}$$

The above expression requires the Jacobian matrix, which we split into horizontal and vertical components based on horizontal and vertical conductivity sensitivities

$$\mathbf{J} = \left\{ \begin{matrix} j^h \\ j^v \end{matrix} \right\}. \quad \text{(A-5)}$$

Here specific elements are given by

$$j_{jk}^h = \frac{\partial d_j^p}{\partial m_{h_k}} \quad \text{and} \quad j_{jk}^v = \frac{\partial d_j^p}{\partial m_{v_k}} \quad j = ,\ldots,N; \quad k = 1,\ldots,M, \quad \text{(A-6)}$$

with N and M representing the number of data points and inverse modeling cells. In terms of the electric field on the simulation mesh Ω_s, the Jacobian elements can also be expressed by

$$j_{jk}^h = \mathbf{q}_j^T \frac{\partial \mathbf{E}}{\partial m_{h_k}} \quad \text{(A-7)}$$

and

$$j_{jk}^v = \mathbf{q}_j^T \frac{\partial \mathbf{E}}{\partial m_{v_k}}, \quad \text{(A-8)}$$

where $\mathbf{q_j}$ is a column vector for the jth data point that maps the electric field solution on Ω_s to the detector location. Next, differentiating equation A-1 with respect to m_{h_k} and m_{v_k}, we have

$$\frac{\partial \mathbf{E}}{\partial m_{h_k}} = \mathbf{K}^{-1}\left(\frac{\partial \mathbf{S}}{\partial m_{h_k}} - \frac{\partial \mathbf{K}}{\partial m_{h_k}}\mathbf{E}\right) \qquad (A\text{-}9)$$

and

$$\frac{\partial \mathbf{E}}{\partial m_{v_k}} = \mathbf{K}^{-1}\left(\frac{\partial \mathbf{S}}{\partial m_{v_k}} - \frac{\partial \mathbf{K}}{\partial m_{v_k}}\mathbf{E}\right). \qquad (A\text{-}10)$$

Using the chain rule, we can express equations A-9 and A-10 in terms of the conductivities on the simulation mesh, where

$$\frac{\partial \mathbf{E}}{\partial m_{h_k}} = \mathbf{K}^{-1}\left(\sum_{l=1}^{P(k)}\frac{\partial \mathbf{S}}{\partial \sigma_{h_l}}\frac{\partial \sigma_{h_l}}{\partial m_{h_k}} - \sum_{l=1}^{P(k)}\frac{\partial \mathbf{K}}{\partial \sigma_{h_l}}\frac{\partial \sigma_{h_l}}{\partial m_{h_k}}\mathbf{E}\right)$$
$$(A\text{-}11)$$

and

$$\frac{\partial \mathbf{E}}{\partial m_{v_k}} = \mathbf{K}^{-1}\left(\sum_{l=1}^{Q(k)}\frac{\partial \mathbf{S}}{\partial \sigma_{v_l}}\frac{\partial \sigma_{v_l}}{\partial m_{v_k}} - \sum_{l=1}^{Q(k)}\frac{\partial \mathbf{K}}{\partial \sigma_{v_l}}\frac{\partial \sigma_{v_l}}{\partial m_{v_k}}\mathbf{E}\right).$$
$$(A\text{-}12)$$

The summations are over conductivity cells on the simulation mesh that overlap cell k on the modeling mesh (Figure A-1). For the kth model (inversion) cell, we have $P(k)$ and $Q(k)$ horizontal and vertical conductivities overlapping from the simulation mesh. For the isotropic case, Commer and Newman (2008) provide an explicit formula for $\partial\sigma_l/\partial m_k$ based on a material averaging scheme of Moskow et al. (1999). The extension to media exhibiting transverse anisotropy is straightforward, with material averaging for horizontal and vertical conductivities each done separately. Computational efficient forms for the gradient (the data part) follow by substituting equations A-11 and A-12 into equations A-7 and A-8 followed by substitution into equation A-4. Note we never explicitly form $\mathbf{K}^{-1}$ or

$$\sigma_h = \left[\int_{x_i}^{x_{i+1}}\left(\int_{z_{k-1/2}}^{z_{k+1/2}}\sigma_h^m(x,z)dz\right)^{-1}dx\right]^{-1}$$
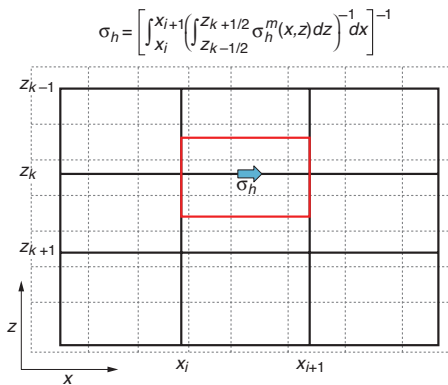

Figure A-1. Concept of separate model/inversion and simulation grids is illustrated in two dimensions. The dashed grid corresponds to the model/inversion mesh Ω_m and the solid grid to the simulation mesh Ω_s. Field simulation on a staggered grid requires that the electrical conductivity be sampled at the edges of the simulation grid; illustrated here is the case for σ_h. The zone outlined in red corresponds to the averaging area on the modeling grid from which σ_h is to be computed on the simulation grid using the aggregation formula from Moskow et al. (1999), shown at the top of the figure.

the Jacobian when evaluating the gradient. For computational efficiency, an adjoint state method is exploited. We refer the reader to Newman and Boggs (2005) for further details.

REFERENCES

Carazzone, J. J., O. M. Burtz, K. E. Green, D. A. Pavlov, and C. Xia, 2005, Three-dimensional imaging of marine CSEM data: 75th Annual International Meeting, SEG, Expanded Abstracts, 575–578.

Carazzone, J. J., T. A. Dickens, K. E. Green, C. Jing, L. A. Wahrmund, D. E. Willen, and M. Commer, and G. A. Newman, 2008, Inversion study of a large marine CSEM survey: 78th Annual International Meeting, SEG, Expanded Abstracts, 644–647.

Commer, M., and G. A. Newman, 2008, New advances in three-dimensional controlled-source electromagnetic inversion: Geophysical Journal International, **172**, 513–535.

——, 2009, Three-dimensional controlled-source electromagnetic and magnetotelluric joint inversion: Geophysical Journal International, **178**, 1305–1316.

Commer, M., G. A. Newman, J. J. Carazzone, T. A. Dickens, K. E. Green, L. A. Wahrmund, D. E. Willen, and J. Shiu, 2008, Massively parallel electrical-conductivity imaging of hydrocarbons using the IBM Blue Gene/L supercomputer: IBM Journal of Research and Development, **52**, no. 1/2, 93–103.

Constable, S., 2006, Marine electromagnetic methods — A new tool for offshore exploration: The Leading Edge, **25**, 438–444.

Eidesmo, T., S. Ellingsrud, L. M. MacGregor, S. Constable, M. C. Sinha, S. Johansen, S. Kong, and F. N. Westerdahl, 2002, Sea bed logging (SBL): A new method for remote and direct identification of hydrocarbon filled layers in deepwater areas: First Break, **20.3**, 144–152.

Ellingsrud, S., T. Eidesmo, S. Johansen, M. C. Sinha, L. M. MacGregor, and S. Constable, 2002, Remote sensing of hydrocarbon layers by seabed logging (SBL): Results from a cruise offshore Angola: The Leading Edge, **21**, 972–982.

Green, K. E., O. M. Burtz, L. A. Wahrmund, T. Clee, I. Gallegos, C. Xia, G. Zelewski, A. A. Martinez, M. J. Stiver, C. M. Rodriguez, and J. Zhang, 2005, R3M case studies: Detecting reservoir resistivity in complex settings: 75th Annual International Meeting, SEG, Expanded Abstracts, 572–574.

Gribenko, A., and M. Zhdanov, 2007, Rigorous 3D inversion of marine CSEM data based on the integral equation method: Geophysics, **72**, no. 2, WA73–WA84.

Hoversten, G. M., G. A. Newman, N. Geier, and G. Flanagan, 2006, 3D modeling of a deepwater EM exploration survey: Geophysics, **71**, no. 5, G239–G248.

Jing, C., K. E. Green, and D. Willen, 2008, CSEM inversion: Impact of anisotropy, data coverage, and initial models: 78th Annual International Meeting, SEG, Expanded Abstracts, 604–607.

Johansen, S. E., H. E. F. Amundsen, T. Røsten, S. Ellingrud, and T. Eidesmo, 2005, Subsurface hydrocarbons detected by electromagnetic sounding: First Break, **23**, 31–36.

Li, M., A. Abubakar, T. Habashy, and Y. Zhang, 2009, Inversion of CSEM data with a model-based inversion algorithm: Geophysical Prospecting, doi: 10.1111/j.1365-2478.2009.00824.x.

Lu, X., and C. Xia, 2007, Understanding anisotropy in marine CSEM data: 77th Annual International Meeting, SEG, Expanded Abstracts, 633–637.

MacGregor, L., D. Andeis, T. Tomlinson, and N. Barker, 2006, Controlled-source electromagnetic imaging of the Nuggets-1 reservoir: The Leading Edge, **25**, 984–992.

MacGregor, L., N. Baker, A. Overton, S. Moody, and D. Bodecott, 2007, De-risking exploration prospects using integrated seismic and electromagnetic data — A Falkland Islands case study: The Leading Edge, **26**, 356–359.

Moskow, S., V. Druskin, T. Habashy, P. Lee, and S. Davdychewa, 1999, A finite difference scheme for elliptic equations with rough coefficients using a Cartesian grid nonconforming to interfaces: SIAM Journal on Numerical Analysis, **36**, no. 2, 442–464.

Newman, G. A., and D. L. Alumbaugh, 2002, Three-dimensional induction logging problems, Part 2: A finite-difference solution: Geophysics, **67**, 484–491.

Newman, G. A., and P. T. Boggs, 2005, Solution accelerators for large-scale three-dimensional electromagnetic inverse problems: Inverse Problems, **20**, S151–S170.

Newman, G. A., and M. Commer, 2008, The influence of electrical anisotropy in 3D marine CSEM surveys: 24th Progress in Electromagnetic Research Symposium, Abstracts, 293.

Plessix, R. E., and P. van der Sman, 2007, 3D CSEM modeling and inversion in complex geological settings: 77th Annual International Meeting, SEG, Expanded Abstracts, 589–593.

Plessix, R.-E., and W. A. Mulder, 2008, Resistivity imaging with controlled-source electromagnetic data: Depth and data weighting: Inverse Problems,

24, 1–22.

Plessix, R. E., and P. van der Sman, 2008, Regularized and blocky 3D controlled source electromagnetic inversion: 24th Progress in Electromagnetic Research Symposium, Abstracts, 755–760.

Tompkins, M., 2005, The role of vertical anisotropy in interpreting marine controlled-source electromagnetic data: 75th Annual International Meeting, SEG, Expanded Abstracts, 514–517.

Tompkins, M., R. Weaver, and L. MacGregor, 2004, Effects of vertical anisotropy on marine active source electromagnetic data and inversions: 66th Conference and Exhibition, EAGE, Extended Abstracts, E026.

Weiss, C. J., and S. Constable, 2006, Mapping thin resistors and hydrocarbons with marine EM methods, Part 2 — Modeling and analysis in 3D: Geophysics, **71**, no 6, G321–G332.

Weiss, C. J., and G. A. Newman, 2002, Electromagnetic induction in a fully 3-D anisotropic earth: Geophysics, **67**, 1104–1114.

Yee, K. S., 1966, Numerical solution of initial boundary value problems involving Maxwell's equations in isotropic media: IEEE Transactions on Antennas and Propogation, **AP-14**, 302–307.

Zach, J. J., A. K. Bjørke, T. Støren, and F. Maaø, 2008, 3D inversion of marine CSEM data using a fast finite-difference time-domain forward code and approximate Hessian-based optimization: 78th Annual International Meeting, SEG, Expanded Abstracts, 614–618.